Petroleum Science 19 (2022) 2199–2209

Contents lists available at ScienceDirect

Petroleum Science

journal homepage: www.keaipublishing.com/en/journals/petroleum-science

Original Paper

Effects of supercritical CO_2 on viscoelastic properties of shales

Da-Wei Zhou [a], Guang-Qing Zhang [a, b, *], Zhong-Wei Huang [a, b], Shi-Yuan Li [a], Zong-Yang Fan [a]

[a] College of Petroleum Engineering, China University of Petroleum in Beijing, Beijing, 102249, China
[b] State Key Laboratory of Petroleum Resources and Engineering, China University of Petroleum in Beijing, Beijing, 102249, China

ARTICLE INFO

Article history:
Received 4 January 2022
Received in revised form
31 May 2022
Accepted 31 May 2022
Available online 3 June 2022

Edited by Yan-Hua Sun

Keywords:
Shale creep
Viscoelastic deformation
SC-CO_2 exposure
Physicochemical mechanisms

ABSTRACT

Laboratory uniaxial compression creep tests, with differential stress of 30 MPa hold for 3 h, were performed on Chang-7, Longmaxi (LMX) and Barnett shales to study the influence of SC-CO_2 on short-term viscoelastic properties. To this end, the wet shale samples were treated with SC-CO_2 with a pressure of 30 MPa and a temperature of 110 °C for 14 days. We analyzed the creep data using the fractional Maxwell model. To investigate microscopic structural alterations, the surface morphology of the same location, before and after SC-CO_2-water exposure, was examined by SEM images. Compared with dry shales, dynamic and static elastic moduli decreased by up to 25.02% and 55.83%, respectively, but the creep deformation increased by 200% for LMX and Chang-7 shales, and 500% for the Barnett shale treated by SC-CO_2. Compared to dry sample, there is an increase in calculated fractional orders of 0.02, 0.07, 0.22 for SC-CO_2 treated samples, indicating that SC-CO_2 treatment is likely to enhance shale creep. SEM investigation confirmed physicochemical mechanisms responsible for the observed elastic damage and creep enhancement, including mineral dissolution and swelling caused by SC-CO_2. This work would further improve our current understanding of the time-dependent deformation of shale under chemical-mechanical coupling effects during CO_2 capture utilization and storage.

1. Introduction

In the context of deep reservoir stimulation, CO_2 has been widely used to displace remaining oil and gas, namely CO_2 enhanced oil recovery (CO_2-EOR) or CO_2 enhanced gas recovery (CO_2-EGR), as well as been stored in unconventional shale reservoirs (Hamza et al., 2020; Wood, 2015; Zhu et al., 2021). Under reservoir conditions, thermal-hydrological-mechanical-chemical interactions between rock and CO_2 significantly affect shale physical-mechanical properties, and it is likely to be the dominant factor for time-dependent deformation during long-term CO_2 injection. Shale creep deformation can cause severe issues, including wellbore instability, proppant embedment, gas production decline, reservoir subsidence, etc. (Du et al., 2018; Feng et al., 2016, 2017). Understanding the time-dependent deformation behavior of shale is still of great importance in addressing the issues in CO_2 capture utilization and storage (CCUS).

It is reported that the rock mineral composition, microstructure, differential stress, temperature, and pore fluid were the key parameters determining rock creep deformation (Brantut et al., 2013). The shale brittle creep behavior has been previously studied on macro- and micro-scale using triaxial/uniaxial or nanoindentation creep tests. In general, the related mechanisms for shale short-term brittle creep may include shear dilation and compaction (Arash et al., 2018; Geng et al., 2017, 2018; Mighani et al., 2019; Xu et al., 2020). Triaxial creep tests on the Ophir shale show that consolidation and volume expansion are always accompanied by primary and secondary creep, respectively. This pre-consolidation and compaction retard the secondary creep rate (Cogan, 1976). Shale as sedimentary rock contains massive clay and organic matter (OM) characterized by numerous bedding planes and micro-pores. Mixed layered clays are often considered a leading source of shale creep due to their viscoelastic behavior of layered structure and micro-pores (Sone and Zoback, 2013). OM, as another significant control of shale creep, can dissipate much energy by dilation and compaction observed from micro-indentation tests (Slim et al., 2019). Some authors have concluded that shale creep tended to increase with the proportion of soft components (clay and OM) and decrease with the proportion of stiff components (quartz, feldspar, pyrite and

* Corresponding author. College of Petroleum Engineering, China University of Petroleum in Beijing, Beijing, 102249, China.
E-mail address: zhangguangqing@cup.edu.cn (G.-Q. Zhang).

https://doi.org/10.1016/j.petsci.2022.05.018

carbonates) (Arash et al., 2018; Liu et al., 2020; Song et al., 2022; Ma et al., 2020; Rassouli and Zoback, 2018; Rybacki et al., 2017; Slim et al., 2019; Sone and Zoback, 2013).

Shale creep deformation is enhanced not only by soft content, differential stress, microstructure, but also by the pore fluid (Almasoodi et al., 2014; Mighani et al., 2019; Rassouli and Zoback, 2020; Rybacki et al., 2017; Sharma et al., 2019; Sone and Zoback, 2014a, b). In a shale reservoir, a portion of water from formation brine and fracturing fluid (less than 20% of flowback (You et al., 2021)) as thin films can remain underground. The injected CO_2 is likely to dissolve into the water resulting in its pH of about 4–5 under simulated reservoir pressure and temperature conditions, showing high chemical reactivity (Rohmer et al., 2016). The physicochemical reactions between CO_2-rich fluid and shale could alter shale compositional, microstructural and mechanical properties, and this further affects the shaly caprock stability and shale gas production (Bhuiyan et al., 2020; Jia et al., 2019; Liu et al., 2012; Sharma et al., 2021). Extensive efforts have been focused on mineral dissolution–precipitation reactions between shale and CO_2-rich fluid. The pore fluid chemically affects fluid adsorption on crack surfaces to extend crack, namely stress corrosion, accelerating the brittle creep strain rate (Brantut et al., 2013; Noël et al., 2021). Shale becomes more compliant and viscous when exposed to water, which is attributed to clay-fluid interactions, electrical double layer repulsion and mineral dissolution (Almasoodi et al., 2014; Du et al., 2018). When CO_2 is introduced into wet shale, swelling–dissolution–precipitation reactions can enhance shale ductility, thus posing potential hazards to fracture conductivity and wellbore stability (Lu et al., 2019; Lyu et al., 2018; Feng et al., 2019; Sharma et al., 2021).

The common creep constitutive models of rock include empirical model, mechanism-based model and component model (Cong and Hu, 2017; Wei et al., 2021; Zhao et al., 2019; Zhang et al., 2015; Zhou et al., 2011). For shale creep models, logarithm function (Chang and Zoback, 2008; Mighani et al., 2019), power-law function (Liang et al., 2020; Rassouli and Zoback, 2018; Rybacki et al., 2017; Sone and Zoback, 2014a, b), and viscoelastic models of Burgers (Li and Ghassemi, 2012) or standard linear solid (Almasoodi et al., 2014) are used to fit the laboratory creep data. Among those models, the empirical model, such as power-law function, was widely used due to fewer parameters inferred from experimental data. Rassouli and Zoback (2018) studied shale creep over both short-term (4-h) and long-term (4-week) periods, indicating that a simple power-law model is capable of describing creep deformation over short and long periods. Liang et al. (2020) further revised the power-law model by incorporating Arrhenius parameters to involve the temperature effect. However, the power-law function as an empirical model, due to a lack of physical foundation and creep mechanism, cannot reasonably predict the long-term viscoelastic creep deformation (Zhou et al., 2011). Although the mechanism-based models can consider influence of micro-crack and damage, parameters need to be determined by the individual, which may result in a large deviation in the result. Therefore, the classical component models, based on a combination of standard elements such as Hooke spring, Newtonian dashpot or even fractional element, are a higher propensity to fit and extrapolate experimental data (Zhou et al., 2011). Both Maxwell and Kevin-Voigt models, composed of elastic springs and viscous dashpots in series and parallel, failed to appropriately represent the time-dependent behavior of shale (Liang et al., 2020). The Maxwell model is unable to capture the nonlinear deformation of shale creep (Rassouli and Zoback, 2018; Sone and Zoback, 2013; Sone and Zoback, 2014a, b). Nevertheless, power-law and Burgers models fit well the creep response of Marcellus shale (Arash et al., 2018). Although the Burgers model yielded better predictions, it is solved in the complicated form of a Maxwell unit (E_1, η_1) and a Voight-Kelvin unit (E_2, η_2). Recently, fractional viscoelastic constitutive equations have been proposed to describe and predict creep behavior of rocks (Di et al., 2011; Peng et al., 2019; Zhou et al., 2013). Because of the precise physical meaning of parameters, decreasing rate and accurate fitting, the fractional model was potentially helpful for explaining rock viscoelastic deformation by identifying only two parameters, i.e., viscosity coefficient and fractional order of the dashpot (Chen and Ai, 2020; Di et al., 2011; Zhou et al., 2011).

To our knowledge, there are relatively few studies focusing on the influence of SC-CO_2 on shale creep deformation. Some crucial questions, including creep deformation revolution and related physicochemical mechanisms when shale is exposed to SC-CO_2, remain unanswered. To this end, we performed uniaxial compression creep and scanning electron microscopy (SEM) experiments on shale samples before and after SC-CO_2 exposure.

2. Methods

2.1. Sample preparation and properties

Three representative shale cores with a diameter of 25 mm and a length of 50 mm, drilled along the direction vertical to the bedding plane, were collected from the outcrop (Fig. 1). They vary largely with respect to composition and fabric due to depositional environments. The Barnett gas shale is taken from one of the largest onshore natural gas fields in the United States, and both marine Longmaxi (LMX) and terrestrial Chang-7 shales are from the highest potential target for unconventional resources in China. Many CO_2-based fracturing and CO_2 enhanced shale gas recovery and sequestration field applications were conducted in shale reservoirs in the past decades (Lyu et al., 2021; Hou et al., 2021). It is of great importance to improve our understanding of time-dependent deformation effects on the performance of gas production and CO_2 sequestration in shale.

A detailed sample characterization and component contents are listed in Table 1. All three samples vary considerably in the proportion of quartz, carbonate, clay and organic matter (OM). The Chang-7 shale contains the most significant content of soft components (clay and OM) up to 47.5%, followed by the Barnett shale with 38.9%, and the LMX shale exhibits the lowest with 23.0%. Among the clay minerals, the proportion of mixed layer illite–smectite as swelling clay can be around 37%, 18% and 12% for Chang-7, LMX and Barnett shales. The chemically reactive carbonate, strongly reacting with CO_2-rich fluid, also varies largely among

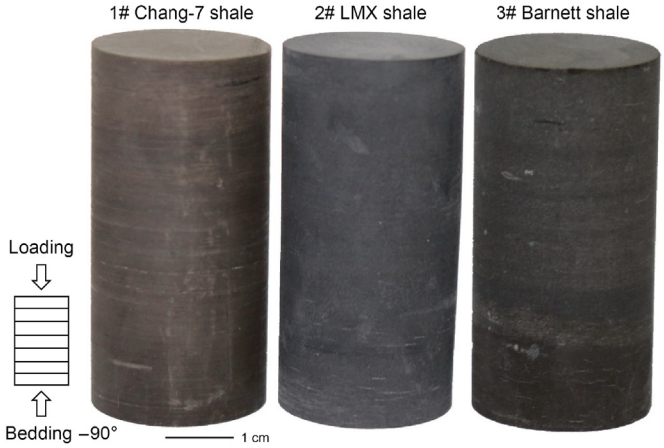

Fig. 1. Photos of cylindrical samples used in experiments.

Table 1
Basic characterizations of three samples.

Sample No.	Sample source	Core length, mm	Core diameter, mm	Dry density, g/cm^3	Mineral content, wt%					
					Quartz	Feldspar	Carbonate	Pyrite	Clay	OM
1	Chang-7	49.86	24.82	2.18	23.3	7.9	6.5	14.8	31.7	15.8
2	LMX	50.02	24.94	2.39	38.0	4.9	30.1	4.0	19.8	3.2
3	Barnett	51.24	25.61	2.46	44.0	2.7	12.4	2.0	32.2	6.7

those shales. So, the selected samples would behave variously on the creep deformation attributed to CO_2-water-shale interactions.

2.2. Experimental procedures

Before introducing water, the "as received" samples were dried for 48 h at 80 °C to remove free water to determine the water content in the following wetting process. Then, to simulate the existence of water film in shale underground, the dried samples were wetted by a high relative humidity of 97.6% formed by K_2SO_4 saturated solution for 26 days under room conditions, leading to 1.37%, 1.42% and 2.36% water content for Chang-7, LMX and Barnett shales. Subsequently, SC-CO_2 with a pressure of 30 MPa and a temperature of 110 °C reacted with wet samples in a high-pressure reactor for 14 days, aiming to study CO_2-shale interactions at a depth of about 3000 m where CO_2 fracturing treatment is applied. To eliminate sample variability, the uniaxial compression creep experiment was conducted on same sample before and after SC-CO_2 exposure, that is, first loading on dry sample (before) and second loading on SC-CO_2 exposed sample (after). SEM images of thin-section samples without a conductive coating were used to examine microscopic structural alterations in the same location with and without SC-CO_2 exposure, revealing possible creep mechanisms. The experimental procedures are detailed as illustrated in Fig. 2. In addition, power X-ray diffraction (XRD) analyses of the LMX shale before and after SC-CO_2-water exposure were carried out to evaluate the chemical and mineralogical changes.

Uniaxial compression creep tests were conducted on a servo-controlled triaxial apparatus of MTS816 under room conditions (Fig. 3(a)). To validate the reliability of the testing system, we conducted uniaxial loading on the aluminum with measured Young's modulus of 70.7 GPa, approaching the standard value of 69 GPa (Fig. 3(b)). Then, uniaxial peak stresses of three kinds of dry shales were obtained. To prevent significant damage in the first creep loading, the applied differential stress level was set for 30 MPa for all three samples, determined from about 45% of σ_p of the weak Chang-7 and Barnett shales. Actually, a brittle creep deformation can be activated when the applied stress is higher than threshold for crack initiation (approximately 40%–60% of σ_p), that is, the onset of dilatant cracking (Brantut et al., 2013). The major challenge of laboratory creep studies of sedimentary rock is to determine minimum reasonable loading time to evaluate and extrapolate creep data. We set the creep loading duration for 3 h that was acceptable, and same creep time can be referred in previous study (Sone and Zoback, 2014a). To calculate the dynamic elastic moduli and identify the damage induced by creep deformation, ultrasonic P- and S-waves with frequency of 1 MHz were recorded along the axial direction with an interval of 1 h.

3. Results

3.1. Creep deformation

Creep curves of three samples before and after SC-CO_2 exposure are shown in Fig. 4. The dry Chang-7 shale behaves largest possibly due to massive soft components (47.5%) and fabrics (Fig. 4(a)). Those soft components in shale were usually considered as a significant source of creep, positively correlated with creep compliance (Sone and Zoback, 2013), and if the proportion of soft components is over 30 wt%, it can principally determine rock ductility (Hamza et al., 2020). In addition, as the clay content increases, the fabrics become more pronounced (Zoback and Kohli, 2019), leading to brittle creep in the form of frictional sliding. The rock brittle creep is primarily driven by microcracking, depending on microstructural state (crack density, porosity, and defect structure), and this exerts a strong influence on the creep strain rate (Brantut et al., 2013). Therefore, the most significant creep deformation obtained for the Chang-7 shale is reasonable due to more soft components and fabrics. On the contrary, the proportion of stiff components is pronounced in LMX shale (77%) and Barnett shale (61.1%), resulting in relatively low creep deformation. After SC-CO_2 exposure, creep deformation increases by approximately 200% for Chang-7 and LMX shales, and 500% for the Barnett shale (Fig. 4(b)). The chemically reactive carbonate minerals, such as calcite and dolomite showing highly chemical activity with CO_2 in the presence of water, are relatively rich in LMX and Barnett shales. Moreover, the microcracks induced by CO_2-water adsorption swelling would cause a significant reduction in shale mechanical properties (Bhuiyan et al., 2020). Therefore, based on the mineral dissolution and clay swelling mechanisms, creep deformation is likely to increase in shale after SC-CO_2 exposure (Fig. 4(b)).

Creep strain rates of three samples are calculated as shown in Fig. 5. Compared to the dry shale, a more significant creep rate is observed in shales after SC-CO_2 exposure. Before SC-CO_2 exposure,

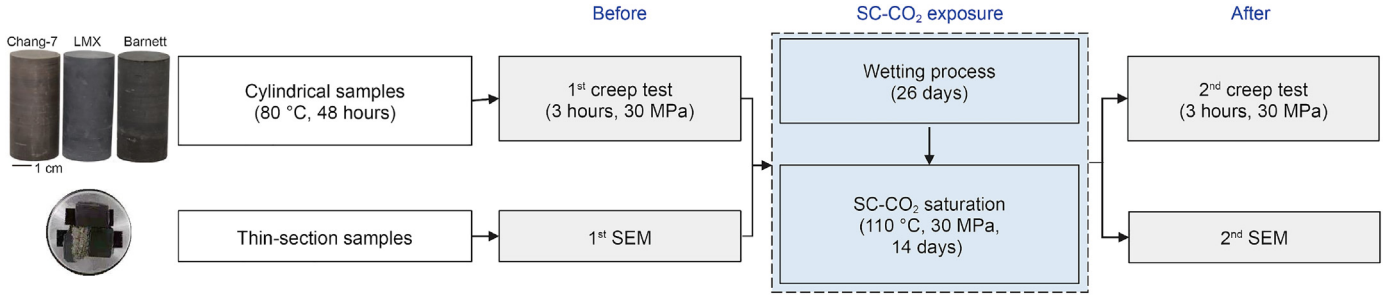

Fig. 2. Schematic flow of sample processing and testing process in this study.

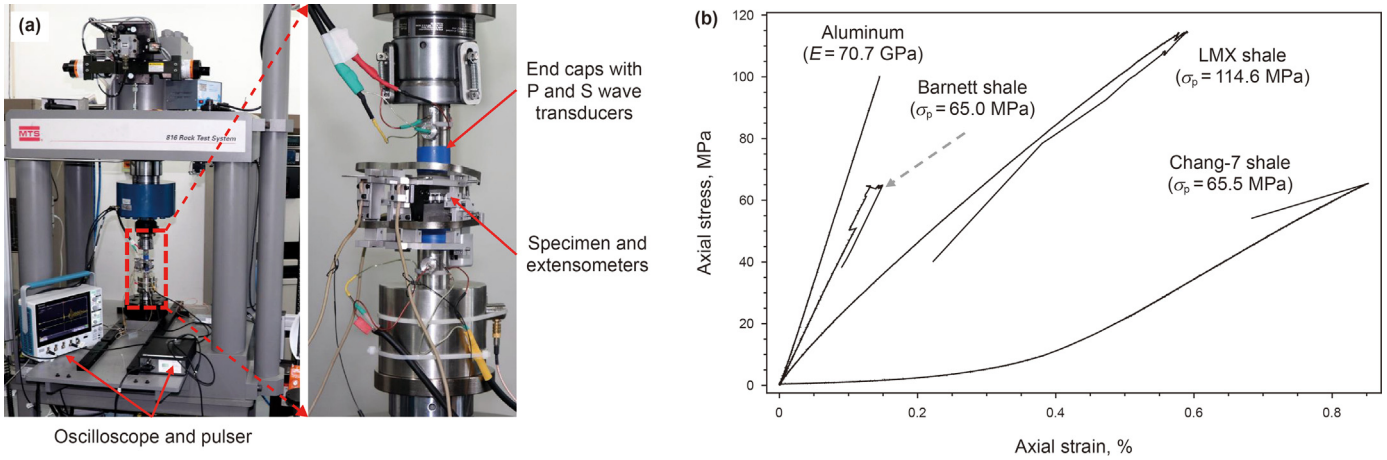

Fig. 3. (**a**) Photos of experimental device used; (**b**) Uniaxial stress-strain curves of aluminum and three types of dry shales. Note that the axial loading rate is 0.02 mm/min using axial control followed by radial control of 0.004 mm/min when the stress is approaching the peak stress.

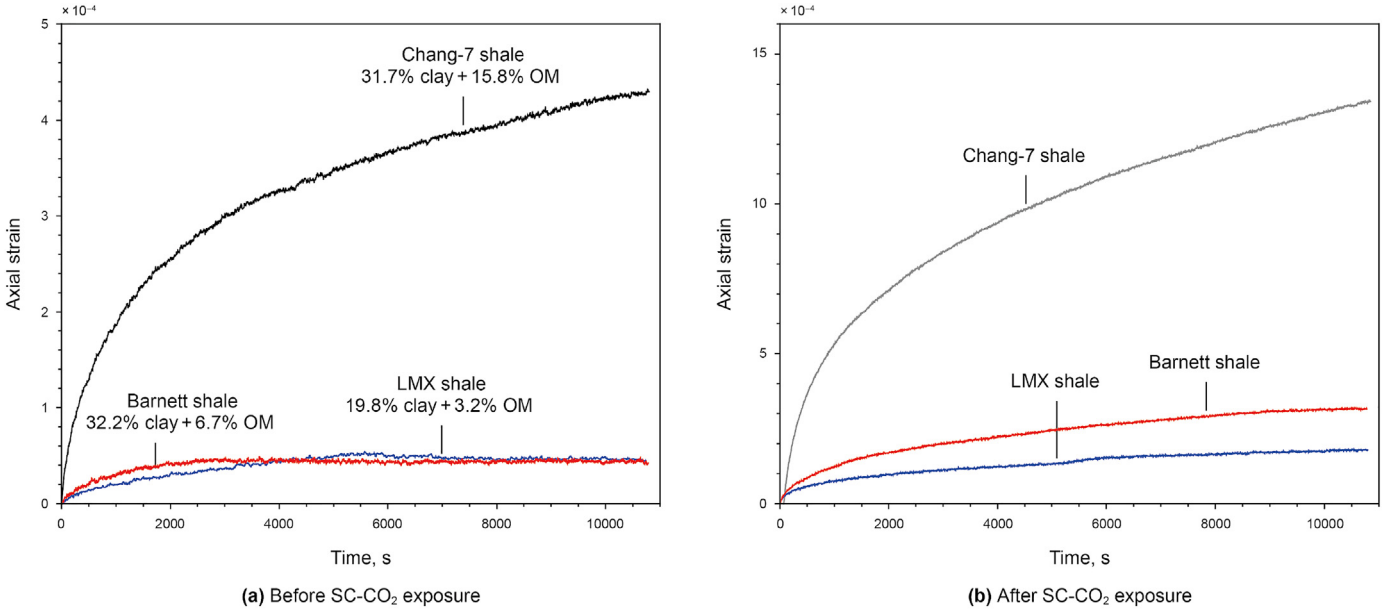

Fig. 4. Curves of creep deformation for Chang-7, LMX and Barnett shales before and after SC-CO_2 exposure.

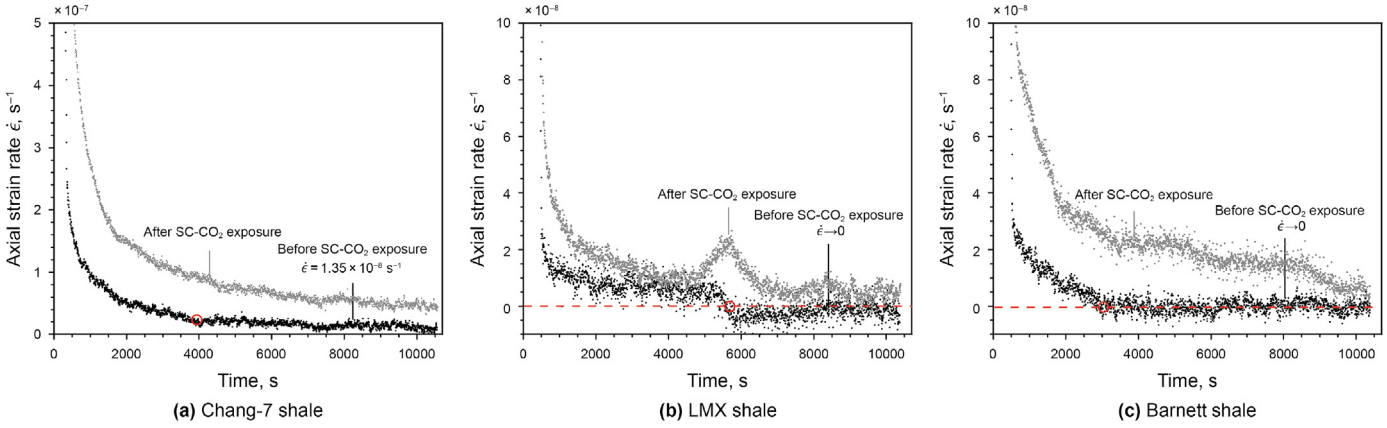

Fig. 5. Creep strain rates for three samples before and after SC-CO_2 exposure. Note that the level of zero strain rate is denoted by a red dashed line, and open red circles show creep transition from primary to second creep for the Chang-7 shale, termination of primary creep without secondary creep for LMX and Barnett shales.

the Chang-7 shale typically exhibits primary (decay) and secondary (steady) creep with a constant rate of about 1.35×10^{-8} s^{-1}, and the transition occurs around 4000 s. There only exists a primary creep stage with a larger decreasing creep rate without entering the secondary creep step for the Chang-7 shale after SC-CO_2 exposure. For both dry LMX and Barnett shales, only primary creep (i.e., the secondary creep rate is zero) can be observed possibly due to the low-stress level (approximately 26% of σ_p for the LMX shale) for crack initiation. After SC-CO_2 exposure, an increase in creep rate is also observed for LMX and Barnett shales. A material with a high level of initial defects, such as microcracks and pores, is expected to creep faster than the same material with a lower level of initial defects (Brantut et al., 2013). We can thus infer that the defects induced by clay swelling and mineral dissolution upon SC-CO_2 saturation enhance the creep strain rate.

3.2. Characterizations of viscoelastic behavior

The Abel dashpot is a fractional derivative description of the Newtonian dashpot, and its constitutive equation is given as (Kiryakova and Al-Saqabi, 1999):

$$\sigma(t) = \eta^{\alpha} \frac{\mathrm{d}^{\alpha} \varepsilon(t)}{\mathrm{d}t^{\alpha}} \quad 0 \le \alpha \le 1 \tag{1}$$

where η^{α} and α are viscosity coefficient and fractional order of dashpot, respectively. The Abel dashpot represents a combination of Newtonian dashpot for an ideal Newtonian fluid ($\alpha = 1$) and Hooke spring for an ideal elastic solid ($\alpha = 0$). Under constant stress for $0 < \alpha < 1$, the strain increases slowly with decreasing rate, indicating that it can describe the rheological behavior of soft materials between fluid and solid. The larger α of material is, the more likely viscous the material behave. When $\sigma(t)$ is equal to a constant (i.e. σ), integrating Eq. (1) using the Riemann-Liouville operator, we can obtain:

$$\varepsilon(t) = \frac{\sigma}{\eta^{\alpha}} \frac{t^{\alpha}}{\Gamma(1+\alpha)} \tag{2}$$

Further inspection of Eq. (2) shows that there are two parameters, α and η^{α}, different from the Newtonian dashpot with only one parameter η. The magnitude of α can be determined by fitting nonlinear laboratory creep strain data using Abel dashpot (Ding et al., 2017; Zhou et al., 2011). To better understand the influence of α on the creep deformation, we plotted a series of creep curves under $\sigma = 30$ MPa and $\eta^{\alpha} = 3$ (GPa h)$^{\alpha}$. We note that creep strain is significantly affected by α, showing a larger creep deformation is induced by a larger α (Fig. 6).

The fractional Maxwell model can be simply formed by only replacing the Newtonian dashpot with the Abel dashpot in the Maxwell model. The time-dependent creep compliance $J(t)$ of fractional Maxwell model is obtained as (Zhou et al., 2011):

$$J(t) = \frac{1}{E_H} + \frac{1}{\eta^{\alpha}} \frac{t^{\alpha}}{\Gamma(1+\alpha)} \tag{3}$$

where Γ is the Gamma function and E_H is the elastic moduli of the Hooke spring.

To fit our creep data, Maxwell model, three-parameter generalized Kelvin model and fractional Maxwell model are chosen (Fig. 7(a)). It is a common method to discard the initial elastic deformation data and use the remaining to precisely derive creep model parameters (Sone and Zoback, 2014a, b), and our data analysis followed the same approach. As observed from Fig. 7, the fractional Maxwell model best fits laboratory data before and after SC-CO_2 exposure. The corresponding fit parameters of three models and estimated variance are given in Table 2. The best fit with the lowest estimated variance is obtained by the fractional Maxwell model, followed by the three-parameter generalized Kelvin model and the Maxwell model. Therefore, we chose the fractional Maxwell model to fit other creep data of LMX and Barnett shales (Fig. 8).

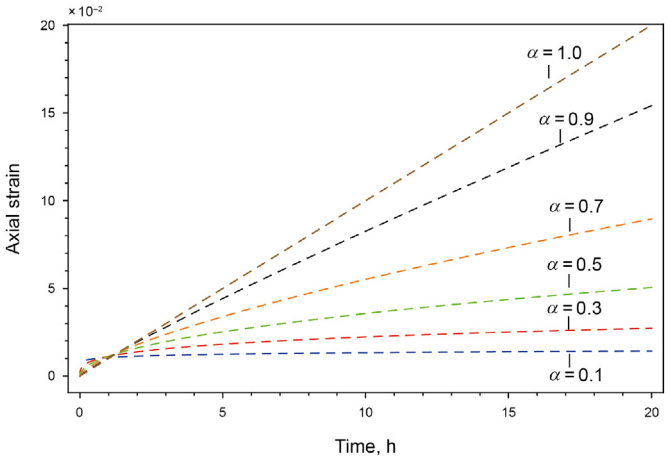

Fig. 6. Creep strain for Abel dashpot model with various α under a case of $\sigma = 30$ MPa and $\eta^{\alpha} = 3$ GPa h$^{\alpha}$.

Based on Eq. (3), the derived fit parameters are listed in Table 3. Except for the dry Barnett shale, the α values are between 0.3 and 0.4 in good agreement with the previous shale creep parameters determined by fractional calculus (Peng et al., 2019). Larger α yields for SC-CO_2 exposed shales, revealing shale becomes more viscous with physical meaning of larger creep deformation under constant loading. Due to various dimensions of η^{α} for shales, the physical description of η^{α} remains unclear. The fractional Maxwell model does not strictly fit well for LMX and Barnett shales without SC-CO_2 exposure, possibly attributed to the low creep stress of Barnett shale and LMX shale anisotropy.

3.3. Static and dynamic elastic moduli

For an isotropic and homogeneous solid material, the dynamic Young's moduli (E_d) can be estimated by ultrasonic wave velocities:

$$E_d = \frac{\rho v_s^2 \left(3v_p^2 - 4v_s^2\right)}{v_p^2 - v_s^2} \tag{4}$$

where ρ is the rock density; v_p and v_s are ultrasonic P- and S-wave velocities, respectively.

As shown in Fig. 9, the cumulative strain of the Chang-7 shale exposed to SC-CO_2 is larger than that of the unexposed. A section of loading curve before creep was used to calculate the static elastic moduli, i.e., Young's moduli (E_s), as listed in Table 4. Compared to dry conditions, E_s is reduced by 55.83% (Chang-7), 33.52% (LMX) and 40.98% (Barnett) after SC-CO_2 exposure. Rock softening caused by the presence of water on elastic properties, compression strength and fracture mechanics, is attributed to fracture surface energy reduction, stress corrosion, fractional reduction and so on (Van Eeckhout, 1976; Zhang et al., 2020; Ma et al., 2021). Introducing CO_2 into wet shale can further promote softening effects largely due to mechano-chemical interactions (Bhuiyan et al., 2020; Liu et al., 2012; Lyu et al., 2018; Rohmer et al., 2016), resulting in shale stiffness degradation.

Ultrasonic waves are generally considered as an effective characterization of rock damage (Geng et al., 2017; Roberts et al., 2015).

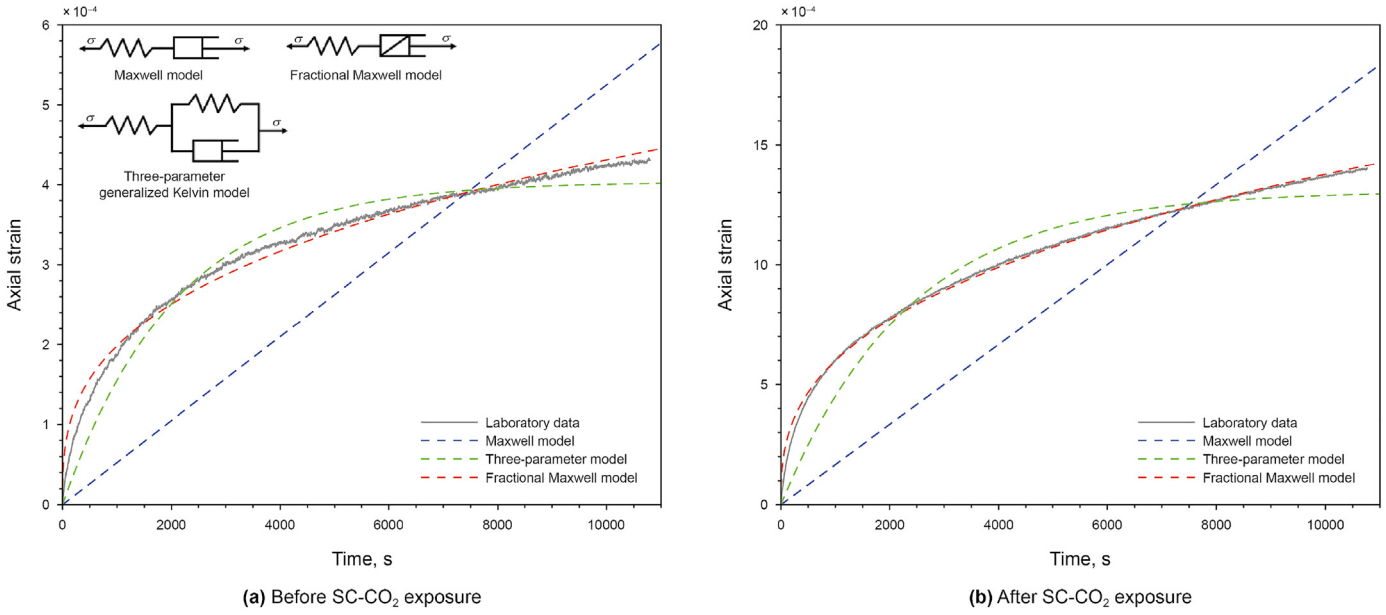

Fig. 7. Creep curves fitted with models without initial elastic data for the Chang-7 shale before and after SC-CO_2 exposure.

Table 2
Estimated parameters of $J(t)$ for different creep models.

Model	Creep compliance $J(t)$	Parameters		Estimated variance, 10^{-10}	
		Before	After	Before	After
Maxwell model	$\frac{1}{E_H}+\frac{t}{\eta_N}$	$\eta_N = 57.0$ GPa s	$\eta_N = 18.0$ GPa s	101.4	879.7
Three-parameter model	$\frac{1}{E_H}+\frac{1}{E_K}\left[1-\exp\left(\frac{E_K}{\eta_K}t\right)\right]$	$E_K = 7.4$ MPa $\eta_K = 15.2$ GPa s	$E_K = 2.3$ MPa $\eta_K = 5.3$ GPa s	3.4	59.3
Fractional Maxwell model	$\frac{1}{E_H}+\frac{1}{\eta^\alpha}\frac{t^\alpha}{\Gamma(1+\alpha)}$	$\alpha = 0.34$ $\eta^\alpha = 172$ (MPa s)$^\alpha$	$\alpha = 0.36$ $\eta^\alpha = 67.9$ (MPa s)$^\alpha$	1.1	2.5

Note: The elastic moduli E_H is not considered due to ignoring initial elastic deformation in our study.

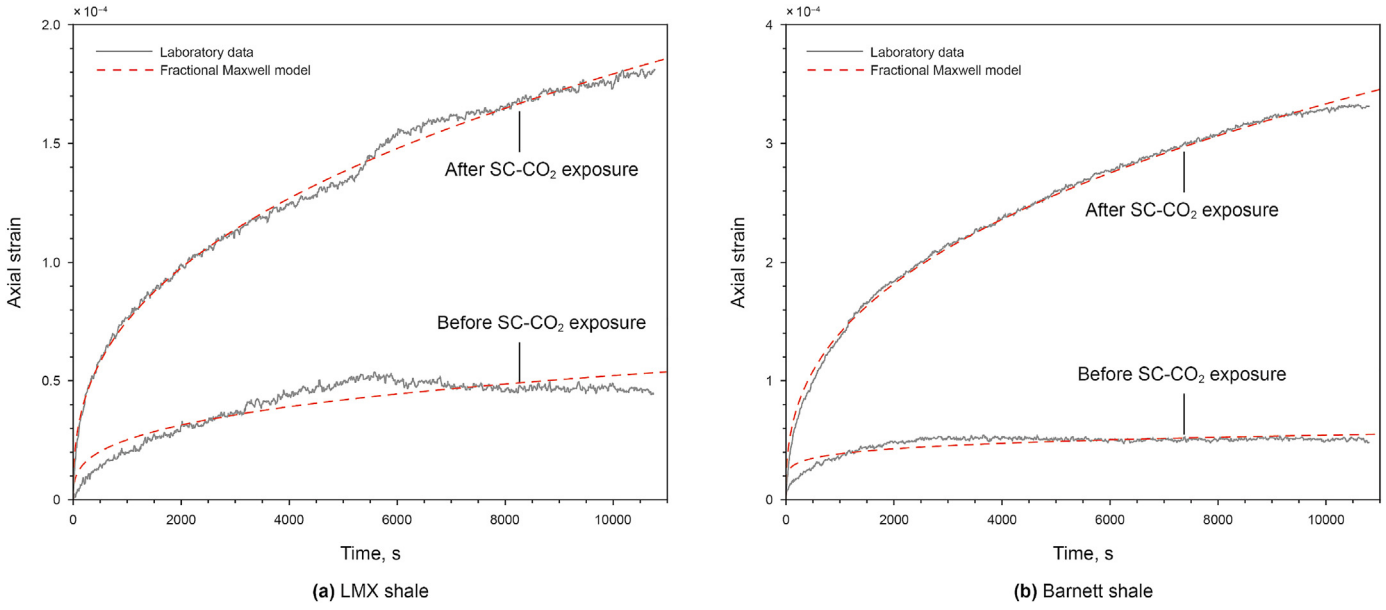

Fig. 8. Creep data of LMX and Barnett shales fitted by fractional Maxwell model.

Table 3
The estimated viscous parameters of the fractional Maxwell model for three samples before and after SC-CO_2 exposure.

Sample	α		η^{α}, (MPa s)$^{\alpha}$	
	Before	After	Before	After
Chang-7	0.34	0.36	173.0	67.9
LMX	0.31	0.38	1240.0	605.0
Barnett	0.15	0.37	230.6	321.4

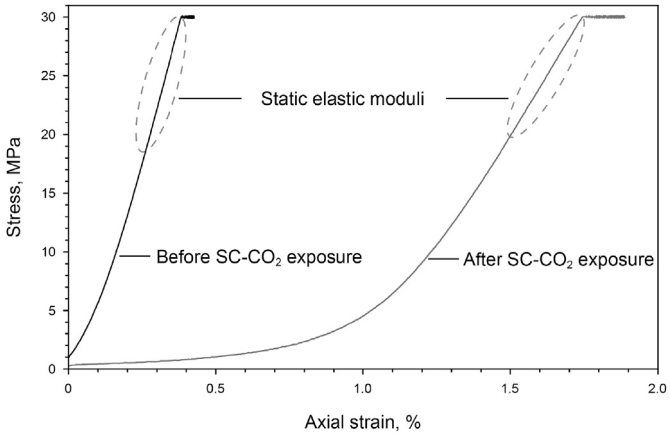

Fig. 9. The typical loading curves of the Chang-7 shale before and after SC-CO_2 exposure.

Table 4
Summary of E_s and E_d of three samples before and after SC-CO_2 exposure.

Sample	E_s, GPa		E_s reduction, %	E_d, GPa		E_d reduction, %
	Before	After		Before	After	
Chang-7	9.32	4.12	55.83	16.18	12.13	25.02
LMX	36.36	24.18	33.52	43.02	41.53	3.46
Barnett	40.78	24.07	40.98	39.48	34.49	12.64

Plots of ultrasonic P- and S- wave velocities during the creep deformation are shown in Fig. 10, showing both v_p and v_s slightly fluctuate around 2% for all samples during the creep loading. So, it is reasonable to neglect the influence of damage induced by the first creep cycle on the second creep cycle. After SC-CO_2 exposure, a reduction of up to 10.9% and 15.4% in both v_p and v_s is observed due to SC-CO_2 reactions. Correspondingly, with respect to E_d, the largest reduction of 25.02% is created for the Chang-7 shale, followed by the Barnett shale with 12.64%, and the LMX shale has the least reduction of 3.46%. The reduction in wave velocities as well as E_d after SC-CO_2 exposure implies that SC-CO_2 can soften rock elastic properties.

3.4. Mechanisms of creep enhanced by SC-CO_2 exposure

To investigate microscopic alterations, shale surface morphology on mm-μm-nm scale was analyzed by SEM images on the same location with and without SC-CO_2-water exposure (Fig. 11). In comparison with the unexposed sample, irreversible alterations are observed after SC-CO_2-water exposure. Macroscopically, bedding plane opening (Fig. 11(a1)) occurs due to crystalline and osmotic swelling of clay exposed to SC-CO_2-water. This phenomenon was also observed in shale exposed to water and SC-CO_2 (Choi and Song, 2012). On the microscale, inter-cracks and intra-cracks are created due to mineral dissolution and deformation inconsistency of various components (Fig. 11(b2), (c4)). Closer microscopic observation shows that significant etching and pitting appear on calcite grain forming microporous media (Fig. 11(c2), (c3)). Similarly, a substantial increase in pore space was observed in carbonate-rich Marcellus shale due to calcium carbonate dissolution (Goodman et al., 2020; Kutchko et al., 2020). Therefore, mineral dissolution and adsorption-induced expansion are the two most essential mechanisms of response for altering the pore structure during the CO_2-shale interactions in the presence of water. These microscopic alterations have the potential to facilitate creep deformation due to an increase in porosity.

It is observed that the content of stiff components (feldspar and carbonate) and clay decreases by about 4 wt% (Fig. 12) due to mineral dissolution, and the SEM images phenomenologically conformed this in Fig. 11. In addition, the content of quartz increases partly due to the reduction of other minerals. Similarly, the same trend of mineral content is supposed to occur in Chang-7 and Barnett shales. Creep compliance is positively correlated with the soft components as well as the porosity, but negatively with the stiff components (Rassouli and Zoback, 2018; Sone and Zoback, 2014a). Meanwhile, carbonate as a stiff component in shale reacts with SC-CO_2, lowering its content and thus stiffness, which results in more compliant behavior with large creep deformation in our experiments.

In addition to the change of mineral composition, the heterogeneity of macro- and micro-fabric of shales significantly affects the deformation behavior, especially for shale exposed to CO_2. After introducing the SC-CO_2-water, the bedding planes tend to open in

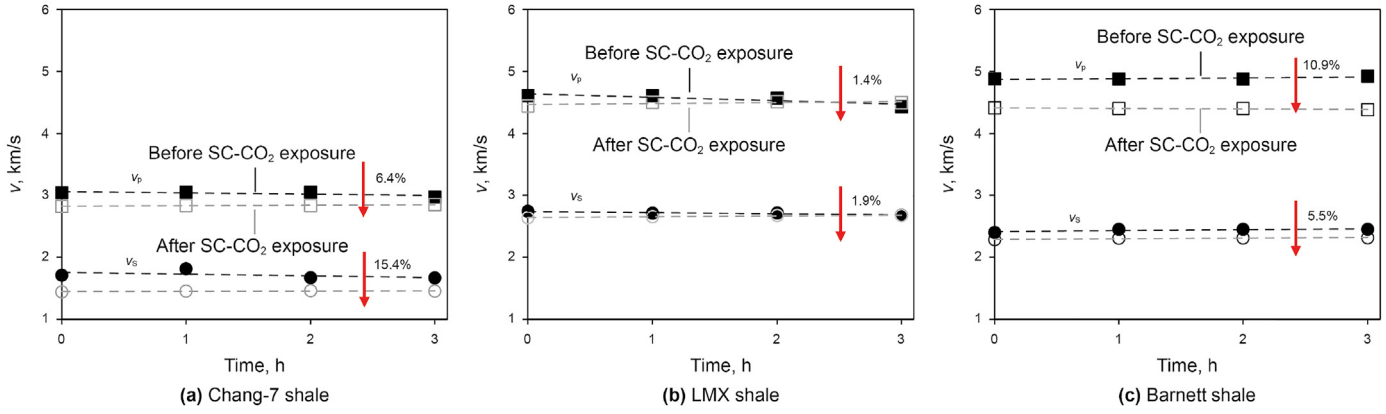

Fig. 10. Ultrasonic P- and S-wave velocities vary with time for three samples before and after SC-CO_2 exposure. The velocities are fitted linearly with dash line, and solid and open symbols represent the data measured on shales before and after SC-CO_2 exposure.

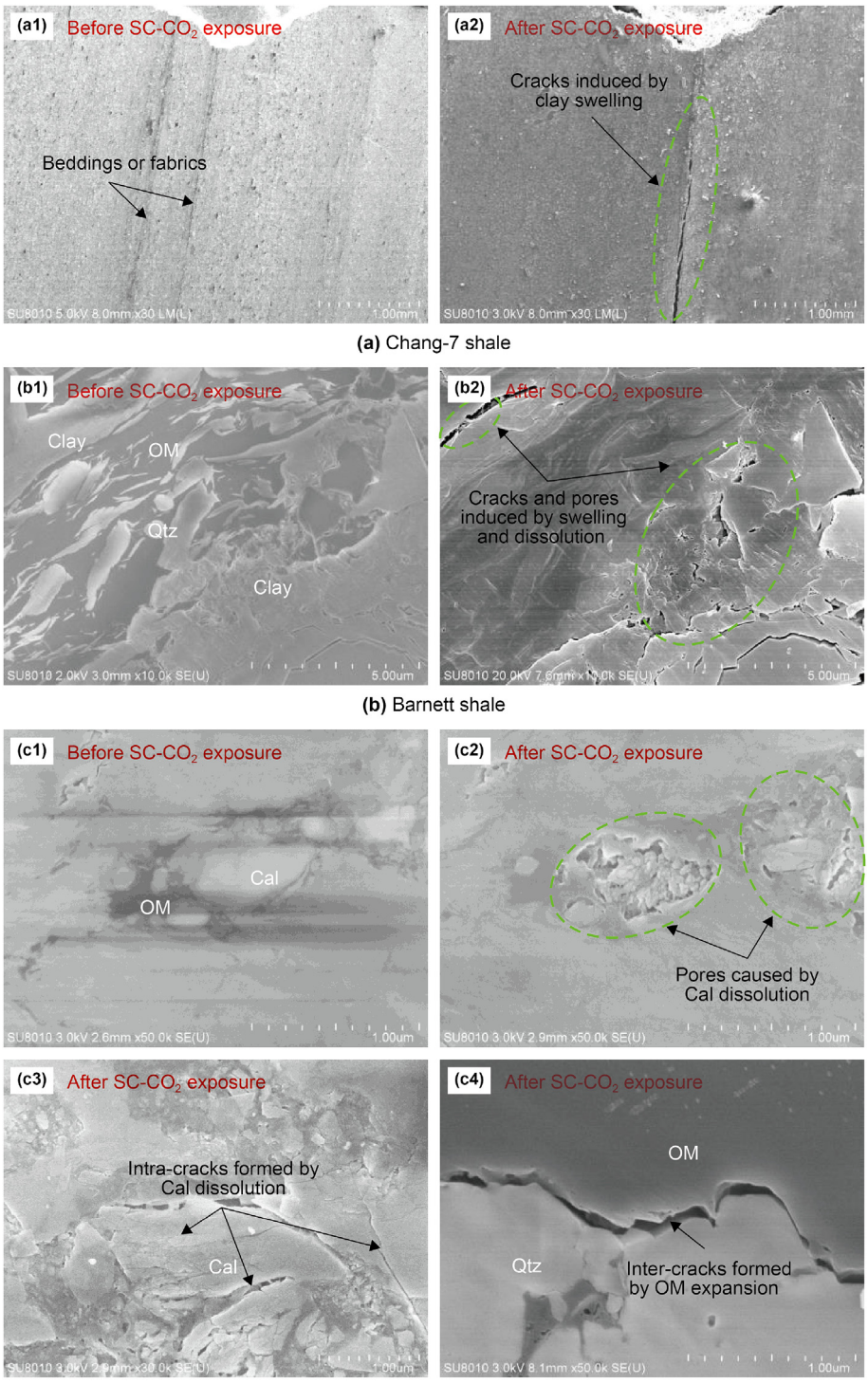

Fig. 11. SEM images of surface morphology of shales exposed to SC-CO_2-water on mm-μm-nm scale. Abbreviations: OM-Organic matter, Cal-Calcite, Qtz-Quartz.

the Chang-7 shale, leading to large creep deformation due to closing the bedding (Fig. 13). Multi-fractures in tensile failure parallel to the uniaxial loading stress are created in the Barnett shale, indicating that the brittle creep failure occurs. So the creep strain of Chang-7 and Barnett samples with various fabrics is primarily accommodated by deformation of the compacting the bedding plane and creating new cracks due to SC-CO_2-water softening effects, respectively. Since the LMX shale is of undeveloped fabrics, the physicochemical reactions failed to cause significant alteration on the micro-macro features, less affecting the creep deformation of shale exposed to SC-CO_2-water.

4. Discussion

4.1. Circumferential strain of creep

Most experimental creep studies have focused on the axial strain but are little concerned with lateral or circumferential

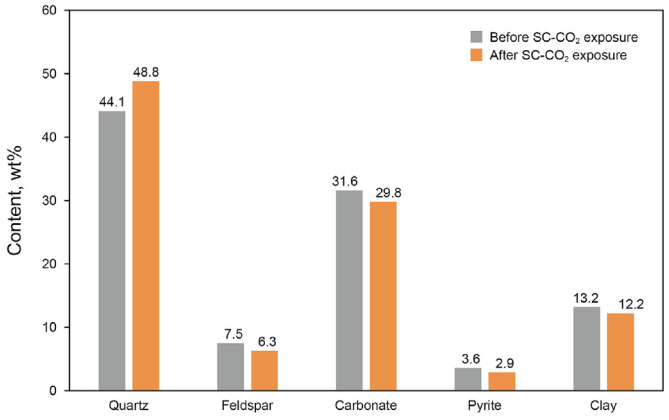

Fig. 12. Change of mineral content of the LMX shale exposed to SC-CO_2-water.

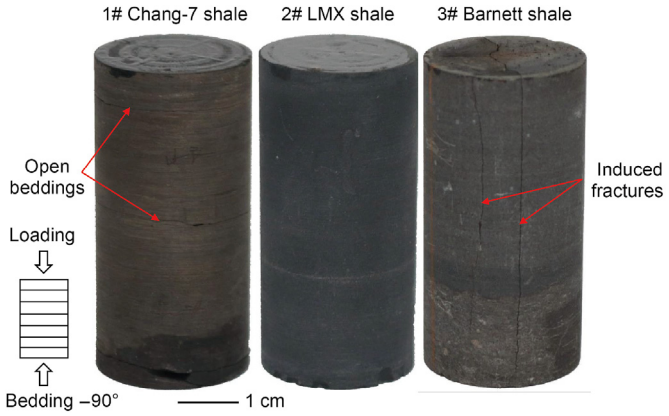

Fig. 13. Features of shale samples after second creep loading.

strains. Fujii et al. (1999) stated that circumferential strain could be used as a condition-insensitive indicator in rock creep experiments. Interestingly, in our experiment, the circumferential strain is more sensitive than the axial strain. We observed three abrupt increases for circumferential strain but no significant related change in axial strain (Fig. 14), possibly indicating that tensile cracks parallel to the loading direction are induced, as shown in Fig. 13. It is known that stress-induced cracks in the form of tensile failure are normally parallel to the loading direction (Stanchits et al., 2006). Only from the axial strain, it is hard to determine the occurrence of tensile failure under uniaxial creep test. So, we argue that axial strain and circumferential strain should be considered simultaneously to characterize shale creep deformation for uniaxial compression creep experiments.

4.2. Mechanical-chemical coupling on shale deformation over geological timescales

Our study showed microscopic alterations of shale structure and mineral components would significantly influence the shale time-dependent deformation. Creep constitutive laws, such as the power-law model (Sone and Zoback, 2014a, b) and fractional Maxwell model (Ding et al., 2017), were used to extrapolate long-term creep deformation based on the laboratory creep data. They included the physical effects of mineral components, stress level and water content on time-dependent rock deformation at the engineering time scale. On-site mechanical-chemical coupling between rock and SC-CO_2 is non-negligible, especially for the long-

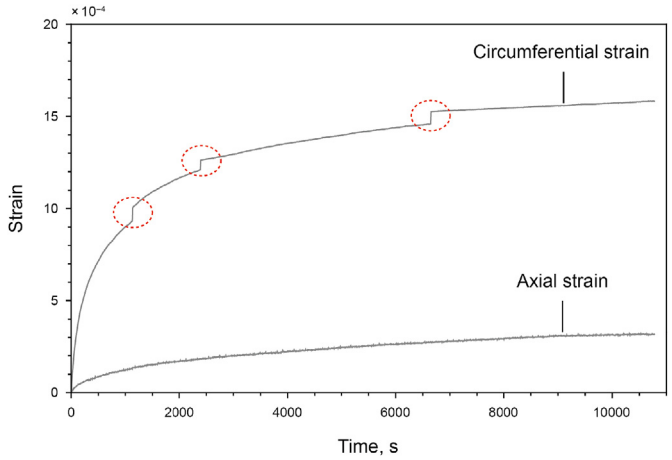

Fig. 14. Axial and circumferential strains for the Barnett shale. The red dashed circles show an abrupt jump in lateral deformation. Note that the circumferential strain is taken as positive for convenient comparison with axial strain.

term scale, significantly changing the mineral component and microstructural state. But in our study, we conducted the creep experiments in the absence of SC-CO_2, different from the coexistence of shale and SC-CO_2 underground, indicating that it is inappropriate to extrapolate laboratory-derived data to tectonic deformation. To date, the commonly used creep constitutive laws for predicting the long-term deformation of shale failed to include the effects of chemical interactions. It is necessary to couple the chemical effects into developing creep models when we extend the laboratory results to the geological issues, such as shaly caprock stability in CCUS (Wood, 2015). Therefore, we need to develop better creep models that describe the effects of mechano-chemical interactions on the brittle creep process.

5. Conclusions

Uniaxial creep experiment and SEM observation were conducted on Chang-7, LMX and Barnett shales before and after SC-CO_2 exposure at a pressure of 30 MPa and a temperature of 110 °C for 14 days. A fractional Maxwell model was optimal to fit creep deformation and evaluate the fit parameters caused by SC-CO_2 effects. Some conclusions are as follows:

(1) Significant elastic damage was induced in shales after SC-CO_2 exposure characterized by a reduction in both dynamic and static elastic moduli. More specifically, the Chang-7 shale showed the largest reduction, followed by the Barnett shale, and the LMX shale exhibiting the lowest reduction in dynamic and static moduli due to composition and fabrics. The SC-CO_2 softening effect was pronounced in the Chang-7 shale, highly dependent on the development of fabrics.

(2) Compared to the dry shale, larger creep deformation and more viscous behavior were considerably induced for SC-CO_2 exposed shale. Creep deformation increased by 200% for LMX and Chang-7 shales, and 500% for the Barnett shale after SC-CO_2 exposure. An increase was also observed in calculated fractional orders of 0.02, 0.07, 0.22 for SC-CO_2 treated samples, indicating that SC-CO_2 is likely to enhance shale viscoelastic properties.

(3) The physicochemical mechanisms for elastic damage and viscous enhancement caused by SC-CO_2 exposure mainly include mineral dissolution and adsorption-induced swelling. These microscopic alterations, mainly created by

carbonate dissolution and clay swelling, increase the porosity to soften shale elastic properties and enhance creep deformation.

Acknowledgments

The authors gratefully acknowledge the support of the National Science Fund for Distinguished Young Scholars (51925405), Beijing Outstanding Young Scientist Program (BJJWZYJH01201911414038), National Natural Science Foundation of China (52104050), China Postdoctoral Science Foundation (2021M703579), National Natural Science Foundation of China (52174011), and China University of Petroleum, Beijing (ZX20200119).

References

Almasoodi, M.M., Abousleiman, Y.N., Hoang, S.K., 2014. Viscoelastic creep of Eagle Ford shale: investigating fluid-shale interaction. In: SPE/CSUR Unconventional Resources Conference. https://doi.org/10.2118/171569-MS.

Arash, K.A., Ehsan, G., Pania, N., Mathew, S., 2018. Elastic, viscoelastic, and strength properties of Marcellus Shale specimens. J. Petrol. Sci. Eng. 171, 662–679. https://doi.org/10.1016/j.petrol.2018.05.074.

Bhuiyan, M.H., Agofack, N., Gawel, K.M., Cerasi, P., 2020. Micro- and macroscale consequences of interactions between CO_2 and shale rocks. Energies 13 (5), 1167. https://doi.org/10.3390/en13051167.

Brantut, N., Heap, M.J., Meredith, P.G., Baud, P., 2013. Time-dependent cracking and brittle creep in crustal rocks: a review. J. Struct. Geol. 52, 17–43. https://doi.org/10.1016/j.jsg.2013.03.007, 2013.

Chang, C., Zoback, M.D., 2008. Creep in unconsolidated shale and its implication on rock physical properties. In: The 42nd U.S. Rock Mechanics Symposium (USRMS). ARMA-08-130.

Chen, Y., Ai, Z., 2020. Viscoelastic analysis of transversely isotropic multilayered porous rock foundation by fractional Poyting-Thomson model. Eng. Geol. 264, 105327. https://doi.org/10.1016/j.enggeo.2019.105327.

Choi, C.S., Song, J.J., 2012. Swelling and mechanical property change of shale and sandstone in supercritical CO_2. In: ISRM Regional Symposium-7th Asian Rock Mechanics Symposium.

Cogan, J., 1976. Triaxial creep tests of Opohonga limestone and Ophir shale. Int. J. Rock Mech. Min. Sci. 13 (1), 1–10. https://doi.org/10.1016/0148-9062(76)90221-7.

Cong, L., Hu, X., 2017. Triaxial rheological property of sandstone under low confining pressure. Eng. Geol. 231, 45–55. https://doi.org/10.1016/j.enggeo.2017.10.005.

Di, Paola, M., Pirrotta, A., Valenza, A., 2011. Visco-elastic behavior through fractional calculus: a easier method for best fitting experimental results. Mech. Mater. 43 (12), 799–806. https://doi.org/10.1016/j.mechmat.2011.08.016.

Ding, X., Zhang, G., Zhao, B., Wang, Y., 2017. Unexpected viscoelastic deformation of tight sandstone: insights and predictions from the fractional Maxwell model. Sci. Rep. 7 (1), 11336. https://doi.org/10.1038/s41598-017-11618-x.

Du, J., Hu, L., Meegoda, J.N., Zhang, G., 2018. Shale softening: observations, phenomenological behavior, and mechanisms. Appl. Clay Sci. 161, 290–300. https://doi.org/10.1016/j.clay.2018.04.033.

Feng, G., Kang, Y., Sun, Z.D., Wang, X.C., Hu, Y.Q., 2019. Effects of supercritical CO_2 adsorption on the mechanical characteristics and failure mechanisms of shale. Energy 173, 870–882. https://doi.org/10.1016/j.energy.2019.02.069.

Feng, Y., Jones, J.F., Gray, K.E., 2016. A review on fracture-initiation and-propagation pressures for lost circulation and wellbore strengthening. SPE Drill. Complet. 31 (2), 134–144. https://doi.org/10.2118/181747-PA.

Feng, Y., Li, X., Gray, K.E., 2017. Development of a 3D numerical model for quantifying fluid-driven interface debonding of an injector well. Int. J. Greenh. Gas Control 62, 76–90. https://doi.org/10.1016/j.ijggc.2017.04.008.

Fujii, Y., Kiyama, T., Ishijima, Y., Kodama, J., 1999. Circumferential strain behavior during creep tests of brittle rocks. Int. J. Rock Mech. Min. Sci. 36 (3), 323–337. https://doi.org/10.1016/S0148-9062(99)00024-8.

Geng, Z., Bonnelye, A., Chen, M., Jin, Y., Dick, P., David, C., Fang, X., Schubnel, A., 2017. Elastic anisotropy reversal during brittle creep in shale. Geophys. Res. Lett. 44 (21). https://doi.org/10.1002/2017GL074555, 10,887-10,895.

Geng, Z., Bonnelye, A., Chen, M., Jin, Y., Schubnel, A., 2018. Time and temperature dependent creep in Tournemire shale. J. Geophys. Res. Solid Earth 123 (11), 9658–9675. https://doi.org/10.1029/2018JB016169.

Goodman, A., Sanguinito, S., Kutchko, B., Natesakhawat, S., Cvetic, P., Allen, A.J., 2020. Shale pore alteration: potential implications for hydrocarbon extraction and CO_2 storage. Fuel 265, 116930. https://doi.org/10.1016/j.fuel.2019.116930.

Hamza, A., Hussein, I.A., Al-Marri, M.J., Mahmoud, M., Aparicio, S., 2020. CO_2 enhanced gas recovery and sequestration in depleted gas reservoirs: a review. J. Petrol. Sci. Eng. 196, 107685. https://doi.org/10.1016/j.petrol.2020.107685.

Hou, L., Zhang, S., Elsworth, D., Liu, H., Sun, B., Geng, X., 2021. Review of fundamental studies of CO_2 fracturing: fracture propagation, propping and permeating. J. Petrol. Sci. Eng. 108823. https://doi.org/10.1016/j.petrol.2021.108823.

Jia, B., Tsau, J.S., Barati, R., 2019. A review of the current progress of CO_2 injection EOR and carbon storage in shale oil reservoirs. Fuel 236, 404–427. https://doi.org/10.1016/j.fuel.2018.08.103.

Kiryakova, V., Al-Saqabi, B., 1999. Explicit solutions to Hyper-Bessel integral equations of second kind. Comput. Math. Appl. 37 (1), 75–86. https://doi.org/10.1016/S0898-1221(98)00243-0.

Kutchko, B., Sanguinito, S., Natesakhawat, S., Cvticz, P., Culp, J., Goodman, A., 2020. Quantifying pore scale and matrix interactions of SC-CO_2 with the Marcellus shale. Fuel 266, 116928. https://doi.org/10.1016/j.fuel.2019.116928.

Li, Y., Ghassemi, A., 2012. Creep behavior of Barnett, Haynesville, and Marcellus shale. In: The 46th U.S. Rock Mechanics/Geomechanics Symposium. ARMA-2012-330.

Liang, Z., Chen, Z., Rahman, S., 2020. Experimental investigation of the primary and secondary creep behaviour of shale gas reservoir rocks from deep sections of the Cooper Basin. J. Nat. Gas Sci. Eng. 73, 103044. https://doi.org/10.1016/j.jngse.2019.103044.

Liu, F., Lu, P., Griffith, C., Hedges, S.W., Soong, Y., Hellevang, H., Zhu, C., 2012. CO_2–brine–caprock interaction: reactivity experiments on Eau Claire shale and a review of relevant literature. Int. J. Greenh. Gas Control 7 (2), 153–167. https://doi.org/10.1016/j.ijggc.2012.01.012.

Liu, K., Rassouli, F.S., Liu, B., Ostadhassan, M., 2020. Creep behavior of shale: nanoindentation vs. triaxial creep tests. Rock Mech. Rock Eng. 54, 321–335. https://doi.org/10.1007/s00603-020-02255-4.

Lu, Y., Chen, X., Tang, J., Li, H., Zhou, L., Han, S., Ge, Z., Xia, B., Shen, H., Zhang, J., 2019. Relationship between pore structure and mechanical properties of shale on supercritical carbon dioxide saturation. Energy 172, 270–285. https://doi.org/10.1016/j.energy.2019.01.063.

Lyu, Q., Tan, J., Li, L., Ju, Y., Bush, A., Wood, D.A., Ranjith, P.G., Middleton, R., Shu, B., Hu, C., Wang, Z., Hu, R., 2021. The role of supercritical carbon dioxide for recovery of shale gas and sequestration in gas shale reservoirs. Energy Environ. Sci. 14, 4203–4227. https://doi.org/10.1039/D0EE03648J.

Lyu, Q., Long, X., Ranjith, P.G., Tan, J., Zhou, J., Wang, Z., Luo, W., 2018. A laboratory study of geomechanical characteristics of black shales after sub-critical/supercritical CO_2+brine saturation. Geomech. Geophy. Geo-Energ. Geo-Resour. 4 (2), 141–156. https://doi.org/10.1007/s40948-018-0079-5.

Ma, D., Cheng, C., Ding, C., Song, J., Hu, D., Zhou, H., 2021. Comparisons of fracturing mechanism of tight sandstone using liquid CO_2 and water. J. Nat. Gas Sci. Eng. 94, 104108. https://doi.org/10.1016/j.jngse.2021.104108.

Ma, Z., Pathegama, Gamage, R., Zhang, C., 2020. Application of nanoindentation technology in rocks: a review. Geomech. Geophy. Geo-Energ. Geo-Resour. 6 (4), 1–27. https://doi.org/10.1007/s40948-020-00178-6.

Mighani, S., Bernabé, Y., Boulenouar, A., Mok, U., Evans, B., 2019. Creep deformation in Vaca Muerta shale from nanoindentation to triaxial experiments. J. Geophys. Res. Solid Earth 124 (8), 7842–7868. https://doi.org/10.1029/2019JB017524.

Noël, C., Passelègue, F.X., Violay, M., 2021. Brittle faulting of ductile rock induced by pore fluid pressure build-up. J. Geophys. Res. Solid Earth 126 (3), e2020JB021331. https://doi.org/10.1029/2020JB021331.

Peng, Y., Zhao, J., Sepehrnoori, K., Li, Y., Li, Z., 2019. The influences of stress level, temperature, and water content on the fitted fractional orders of geomaterials. Mech. Time-Dependent Mater. 24, 221–232. https://doi.org/10.1007/s11043-019-09417-0.

Rassouli, F.S., Zoback, M.D., 2020. Preliminary results on multi-stage creep experiments of the Wolfcamp shale at elevated temperature. In: 54th U.S. Rock Mechanics/Geomechanics Symposium. ARMA-2020-1577.

Rassouli, F.S., Zoback, M.D., 2018. Comparison of short-term and long-term creep experiments in shales and carbonates from unconventional gas reservoirs. Rock Mech. Rock Eng. 51 (7), 1995–2014. https://doi.org/10.1007/s00603-018-1444-y.

Roberts, L.A., Buchholz, S.A., Mellegard, K.D., Düsterloh, U., 2015. Cyclic loading effects on the creep and dilation of salt rock. Rock Mech. Rock Eng. 48 (6), 2581–2590. https://doi.org/10.1007/s00603-015-0845-4.

Rohmer, J., Pluymakers, A., Renard, F., 2016. Mechano-chemical interactions in sedimentary rocks in the context of CO_2 storage: weak acid, weak effects? Earth Sci. Rev. 157, 86–110. https://doi.org/10.1016/j.earscirev.2016.03.009.

Rybacki, E., Herrmann, J., Wirth, R., Dresen, G., 2017. Creep of Posidonia shale at elevated pressure and temperature. Rock Mech. Rock Eng. 50 (12), 3121–3140. https://doi.org/10.1007/s00603-017-1295-y.

Sharma, S., Agrawal, V., McGrath, S., Hakala, J.A., Lopano, C., Goodman, A., 2021. Geochemical controls on CO_2 interactions with deep subsurface shales: implications for geologic carbon sequestration. Environ. Sci.: Process. Impacts 23, 1278–1300. https://doi.org/10.1039/D1EM00109D.

Sharma, P., Prakash, R., Abedi, S., 2019. Effect of temperature on nano-and micro-scale creep properties of organic-rich shales. J. Petrol. Sci. Eng. 175, 375–388. https://doi.org/10.1016/j.petrol.2018.12.039.

Slim, M., Abedi, S., Taras Bryndzia, L., Ulm, F., 2019. Role of organic matter on nanoscale and microscale creep properties of source rocks. J. Eng. Mech. 145 (1). https://doi.org/10.1061/(ASCE)EM.1943-7889.0001538.

Sone, H., Zoback, M.D., 2013. Mechanical properties of shale-gas reservoir rocks—Part 2: Ductile creep, brittle strength, and their relation to the elastic modulus. Geophysics 78 (5), D393–D402. https://doi.org/10.1190/geo2013-0051.1.

Sone, H., Zoback, M.D., 2014a. Time-dependent deformation of shale gas reservoir rocks and its long-term effect on the in situ state of stress. Int. J. Rock Mech. Min. Sci. 69, 120–132. https://doi.org/10.1016/j.ijrmms.2014.04.002.

Sone, H., Zoback, M.D., 2014b. Viscous relaxation model for predicting least principal stress magnitudes in sedimentary rocks. J. Petrol. Sci. Eng. 124, 416–431.

https://doi.org/10.1016/j.petrol.2014.09.022.
Song, J., Xiang, D., Hu, D., Zhou, H., Guo, D., Zhang, G., 2022. Creep characteristics of a fracturing fluid-softened shale investigated by microindentation. Int. J. Rock Mech. Min. Sci. 152, 105067. https://doi.org/10.1016/j.ijrmms.2022.105067.
Stanchits, S., Vinciguerra, S., Dresen, G., 2006. Ultrasonic velocities, acoustic emission characteristics and crack damage of basalt and granite. Pure Appl. Geophys. 163 (5), 975–994. https://doi.org/10.1007/s00024-006-0059-5.
Van Eeckhout, E.M., 1976. The mechanisms of strength reduction due to moisture in coal mine shale. Int. J. Rock Mech. Min. Sci. 13 (2), 61–67. https://doi.org/10.1016/0148-9062(76)90705-1.
Wei, Y., Chen, Q., Huang, H., Xue, X., 2021. Study on creep models and parameter inversion of columnar jointed basalt rock masses. Eng. Geol. 290 (3), 106206. https://doi.org/10.1016/j.enggeo.2021.106206.
Wood, D.A., 2015. Carbon dioxide (CO_2) handling and carbon capture utilization and sequestration (CCUS) research relevant to natural gas: a collection of published research (2009–2015). J. Nat. Gas Sci. Eng. 25, A1–A9. https://doi.org/10.1016/j.jngse.2015.05.013.
Xu, J., Tang, X., Wang, Z., Feng, Y., Bian, K., 2020. Investigating the softening of weak interlayers during landslides using nanoindentation experiments and simulations. Eng. Geol. 277, 105801. https://doi.org/10.1016/j.enggeo.2020.105801.
You, L., Zhang, N., Kang, Y., Xu, J., Cheng, Q., Zhou, Y., 2021. Zero flowback rate of hydraulic fracturing fluid in shale gas reservoirs: concept, feasibility, and significance. Energy Fuels 35 (7), 5671–5682. https://doi.org/10.1021/acs.energyfuels.1c00232.
Zhang, G., Wu, Y., Wang, L., Zhang, K., Daemen, J., Liu, W., 2015. Time-dependent subsidence prediction model and influence factor analysis for underground gas storages in bedded salt formations. Eng. Geol. 187, 156–169. https://doi.org/10.1016/j.enggeo.2015.01.003.
Zhang, G., Zhou, D., Wang, P., Zhangz, K., Tang, M., 2020. Influence of supercritical CO_2-water on the micromechanical properties of sandstone. Int. J. Greenh. Gas Control 97, 103040. https://doi.org/10.1016/j.ijggc.2020.103040.
Zhao, J., Feng, X., Zhang, X., Yang, C., 2019. Brittle and ductile creep behavior of Jinping marble under true triaxial stress. Eng. Geol. 258, 105157. https://doi.org/10.1016/j.enggeo.2019.105157.
Zhou, H., Wang, C., Han, B., Duan, Z., 2011. A creep constitutive model for salt rock based on fractional derivatives. Int. J. Rock Mech. Min. Sci. 48 (1), 116–121. https://doi.org/10.1016/j.ijrmms.2010.11.004.
Zhou, H., Wang, C., Mishnaevsky, L., Duan, Z., Ding, J., 2013. A fractional derivative approach to full creep regions in salt rock. Mech. Time-Dependent Mater. 17 (3), 413–425. https://doi.org/10.1007/s11043-012-9193-x.
Zhu, C.F., Guo, W., Wang, Y.P., Li, Y.J., Gong, H.J., Xu, L., Dong, M.Z., 2021. Experimental study of enhanced oil recovery by CO_2 huff-n-puff in shales and tight sandstones with fractures. Petrol. Sci. 18 (3), 852–869. https://doi.org/10.1007/s12182-020-00538-7.
Zoback, M.D., Kohli, A.H., 2019. Unconventional Reservoir Geomechanics. Cambridge University Press.